Journal of Astronomical Telescopes, Instruments, and Systems

AstronomicalTelescopes.SPIEDigitalLibrary.org

Uniformity and stability of the LSST focal plane

Paul O'Connor

SPIE.

Paul O'Connor, "Uniformity and stability of the LSST focal plane," *J. Astron. Telesc. Instrum. Syst.* **5**(4), 041508 (2019), doi: 10.1117/1.JATIS.5.4.041508.

Uniformity and stability of the LSST focal plane

Paul O'Connor*
Brookhaven National Laboratory, Instrumentation Division, Upton, New York, United States

Abstract. The Large Synoptic Survey Telescope (LSST) focal plane consists of 21 autonomous modules [raft tower modules (RTMs)], each of which contains nine thick, fully depleted 4k × 4k CCDs with associated control and readout electronics. To enable LSST's repetitive short-exposure cadence while maintaining high duty factor and low read noise, the readout is highly parallelized into 3024 independent video channels (16 per CCD and 144 per RTM). Two vendors supplied the LSST sensors; the devices have compatible mechanical and electrical interfaces and meet the same electro-optic specifications, but each RTM is constructed with sensors from a single supplier. The full complement of rafts was assembled at Brookhaven National Laboratory during January 2017 to January 2019. Each unit underwent extensive electro-optic and metrology characterization at operating temperature, the results of which are presented here along with a discussion of uniformity and stability. [DOI: 10.1117/1.JATIS.5.4.041508]

Keywords: LSST; CCDs; CCD readout.

Paper 19034SS received Apr. 5, 2019; accepted for publication Sep. 16, 2019; published online Oct. 11, 2019.

1 Introduction

The Large Synoptic Survey Telescope (LSST) is a next-generation imaging instrument with 320 m^2 deg^2 etendue, designed to carry out a 10-year survey targeting dark matter and dark energy, solar system and Milky Way populations, and optical transients.[1] The 3.2-Gpixel LSST camera, developed by a US Department of Energy collaboration, will have a science array of 189 fully depleted CCDs arranged in 21 submodules called raft tower modules (RTMs)[2,3] making it the largest digital camera thus far built for astronomical research. LSST's survey cadence involves covering the sky in repeated short exposures, making it necessary to minimize the closed-shutter readout time in addition to maximizing throughput across the 350- to 1050-nm wavelength band. Table 1 compares the LSST focal plane with other recent large imaging cameras.

The science array is arranged as a set of 21 autonomous, fully testable modules each containing nine fully depleted 4k × 4k CCDs together with all CCD control and video processing electronics contained in a compact, cryostat-compatible enclosure. A diagram of the focal plane layout and a photograph of one assembled RTM are shown in Fig. 1.

1.1 *Sensors and Electronics*

Key requirements for the LSST sensors were formulated early in the project, and a multiyear prototyping program was carried out with several suppliers. The production devices are of two types, the CCD-250 made by Teledyne-e2v (henceforth E2V) and the STA3800C, designed by Semiconductor Technology Associates, wafers fabricated at Teledyne-DALSA, and devices postprocessed, packaged, and tested at the Imaging Technology Laboratory (ITL) of the University of Arizona. Both devices share a common 4k × 4k pixel format, 10-μm^2 pixels, with 16 independently read out amplifier segments of 512 × 2k pixels. Devices are back-illuminated and fabricated on high-resistivity p-type silicon thinned to 100 μm, which is sufficient to meet the y band throughput requirement without introducing enough charge diffusion to impact the point spread function.[8,9] Devices have four-side buttable packages and achieve >90% fill factor including nonimaging silicon area and interchip gaps. The two device types are 100% interchangeable in their mechanical and electrical interfaces to the RTM but differ in their construction (see Table 2).

Both devices are treated with proprietary coatings on the entrance side and the substrate-facing side, leading to differences in quantum efficiency (QE) at various wavelengths. Finally, ITL device outputs are buffered by JFET source followers mounted on the flex cables that interface the sensor to the RTM electronics boards. These were found to be necessary to provide sufficiently fast video rise and fall times to meet the 2-s frame readout requirement.

To accommodate the high number of video channels in the LSST focal plane, each RTM incorporates a compact, ASIC-based control, and readout electronics system[10] on three PC boards occupying the ∼4-L volume in the shadow of the CCD subarray. The RTM electronics includes 144 channels of video processing (amplification, dual-slope integration filtering, 18-bit digitization, data multiplexing, and serial output link), CCD bias, timing, and control signal generation, thermal control of the CCD array, power conditioning, and monitoring and readback of several hundred temperatures, voltages, and currents. A strict power budget of <50 W (average) is necessary to match the heat removal capacity of the cryostat refrigeration system.

1.2 *Electro-Optic Performance Requirements and Production Test Methods*

The performance requirements for the RTM are summarized in Table 3.

Since each RTM is able to function as standalone camera, the RTM electro-optic test stand has been built to simulate, as closely as possible, the conditions that will be experienced in the final LSST focal plane: early versions of the camera control[11] and data acquisition[12] software are used to execute exposure sequences, substantial use is made of the LSST data

*Address all correspondence to Paul O'Connor, E-mail: poc@bnl.gov

2329-4124/2019/$28.00 © 2019 SPIE

Table 1 Imaging focal plane array comparison

Instrument	Camera	Science CCDs	Pixel count	Video channels	Readout time (s)
Pan-STARRS 1	GPC-1[4]	60	1.44G	480	7
Dark energy survey	DECam[5]	62	504M	124	20
Subaru	Hyper Suprime-Cam[6]	104	872M	208	20
LSST	LSSTCam[7]	189	3.024G	3024	2

Table 2 Construction differences between sensor types.

	E2V	ITL
Parallel clock phases	4	3
Output amplifier	2-stage	1-stage
Entrance window	Implant	Chemisorption
Package style	Cantilevered Si wirebonded	In bump bonded
Antiblooming stop	Yes	No
Tip/tilt/piston control	Shims	Precision jig used during epoxy bonding

management software stack[13] for image analysis, and prototype LSST power supplies are used. RTMs are housed in a vacuum cryostat with cold plates held at −130°C and −60°C to remove heat from the sensor array and electronics, respectively. (The LSST camera will hold the electronics cold plate at −40°C, but our commercial closed-cycle cryocooler does not have sufficient cooling capacity at the higher temperature.)

The EO test methods follow conventional procedures for CCD characterization such as those described in Ref. 14. CCD clock and bias voltages and timing sequences were set to the manufacturer's suggested values. In early raft testing, some variations around the standard settings were explored; additional work to optimize performance[15] is underway but is a separate activity from the production tests reported here. Key measurements that are made are: (1) ^{55}Fe exposures, providing measurements of gain (by fitting the Mn-K_α and K_β lines for reconstructed clusters), noise (from overscan pixels), and charge diffusion (from cluster sizes); (2) dark exposures of 500 s; (3) monochromatic flatfields from 350 to 1100 nm for QE; (4) monochromatic flatfield pairs at increasing exposure times for linearity, full-well capacity, and photon transfer curve; (5) superflat exposures, coadded to produce low-noise files suitable for charge transfer efficiency measurements using the extended pixel edge response method;[14] and (6) 12- to 20-h runs with continuous ^{55}Fe exposures, to estimate response stability. Note that according to our test specification, full well is defined as the maximum output signal level, not the signal level in which the charge transfer breaks down. Also in keeping with general practice, the "gain" of a channel is expressed in e-/ADU (actually an inverse gain). For most rafts, EO runs were carried out at two CCD temperatures (−90°C and −100°C); results given in subsequent sections are for −90°C temperature.

The tests described here have been developed to verify, using fully automated acquisition and analysis, that the LSST science rafts satisfy the performance criteria in Table 3. Further studies of subtle characteristics (persistence, crosstalk, distortions due to static and dynamic electrostatic effects, etc.) have been carried out on single CCDs and are reported in Refs. 16–19.

2 Uniformity Results

2.1 *Quantum Efficiency*

QE measurement uses conventional methods[20] and is referenced to a NIST-calibrated photodiode and corrected for flatfield irradiance falloff across the raft surface. A single number is reported for each CCD by averaging the response after correcting the individual segments' gain and offset. Spatial nonuniformity of QE across the CCD surface is typically at the 1% level in midband, up to 3% RMS below 450 nm and above 950 nm due to window processing and fringing, respectively. Figure 2 shows the QE curves for all CCDs, separated by supplier type.

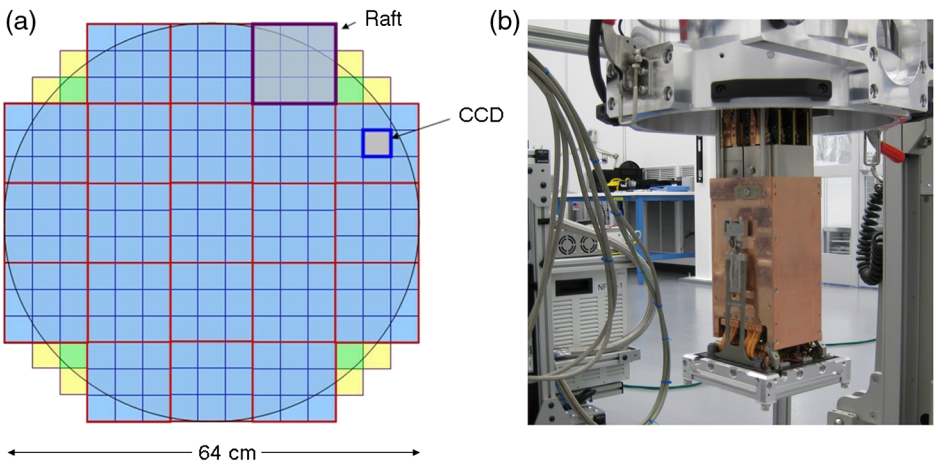

Fig. 1 (a) Arrangement of CCDs and RTMs in the LSST science focal plane and (b) assembled RTM being inserted into test cryostat. CCD subarray, downward-facing in this view, is covered by aluminum protective frame.

Table 3 RTM electro-optic performance requirements and measured median performance for the 189 CCDs, 3024 video channels on 21 rafts

Parameter	Requirement (threshold)	Measured (median of 21 RTMs)	Unit
QE-u	≥41	68	%
QE g	≥78	89.4	%
QE-r	≥88	95.2	%
QE–i	≥81	98.4	%
QE-z	≥75	87.5	%
QE-y	≥21	29.9	%
Diffusion	≤5.0	4.20	μm rms
Dark current (95th-percentile)	≤0.2	0.017	e^-/pix/s
Unusable pixels	≤1.0	0.095	%
Frame read time (144 Mpix)	≤2	1.94	s
Read noise	≤9 (13)	4.84	e^- rms
CTI serial (at 1ke^- signal)	≤5 (30)	1.6	ppm
CTI parallel (at 1ke^- signal)	≤3	0.6	ppm
Power dissipation	58.2	39	W
Electronic crosstalk	2	0.08 (typ.)	%

Standard deviations of the parameters are given in Table 4. QE, quantum efficiency and CTI, charge transfer inefficiency. Numbers in parentheses are allowances defined by the project that either restrict the fractional distribution of noncompliant channels or impose secondary tests to ensure that science goals will not be impacted

Absolute QE numbers have uncertainties of 2% to 5%, whereas relative variations include instrumental drifts over the 28-month production period. In general, there is higher QE at low and high wavelengths for E2V and ITL sensors, respectively.

2.2 *Noise, Full Well, Dark Current, Charge Diffusion, Charge Transfer Inefficiency*

Figure 3 shows the distribution of parameters for the 189 CCDs (3024 channels) of the focal plane, separated by CCD supplier. Population statistics are summarized in Table 4. Figure 4 shows RTM-by-RTM parameter distributions.

In contrast to the QE results, the electro-optic parameters show a greater difference between CCD types, with nearly non-overlapping distributions in some cases. Furthermore, the ITL sensors show greater variability in parameters. Figure 5 shows that the read noise and full-well parameter differences are linked through the different gains of the two CCD types. Gain, read noise, and full well are all governed by the sense node capacitance,[14] which apparently differs by roughly 35% between the two suppliers. The electronic gain can be controlled at the CCD level and will be adjusted during operation to ensure that the maximum CCD signal does not saturate the ADC, as this is necessary for accurate crosstalk correction.

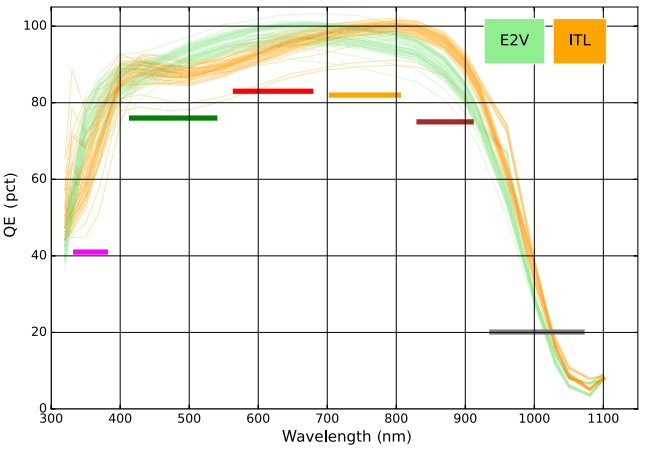

Fig. 2 QE versus wavelength for E2V (green) and ITL (orange) sensors (72 sensors of each type). Horizontal (magenta, green, red, yellow, brown, and gray) lines indicate the passbands and band-averaged QE requirements for (u, g, r, i, z, and y) filters.

2.3 *Correlated Noise and Effect of Reduced Readout Rate*

In order to read out the CCDs in 2 s, their serial registers are clocked at a relatively rapid rate of 545 kHz, leaving little timing margin in the readout sequence to isolate CDS integration intervals from nearby clock transitions. We made two observations that suggested that clock-coupled noise was present in some devices. First, clock feedthrough was seen to be pronounced in video waveforms of the noisier devices. Second, measurements were made, which showed significant correlation between the noise waveforms of the 16 channels of individual CCDs. (See Fig. 6. Since we record the waveforms of all 144 raft video channels, we can calculate their pairwise correlation coefficients while readout out a bias image.) Comparison of the degree of intra-CCD correlation and read noise (Fig. 7) confirmed the connection.

We also observed that read noise could be reduced by adding delays between the clock edges and the integration intervals while keeping the integration times constant. For RTM-10, we varied the timing to give frame readout times of 2, 3, 4, and 5 s; both the noise and the dispersion in noise decreased [Fig. 8(a)]. Thirteen rafts were then measured at both 2- and 3-s readout times. An improvement of 10% to 20% was found for the slower readout, with the noisiest channels on ITL devices benefiting the most [Fig. 8(b)].

3 Stability Results in Test Cryostat

For each raft, a long-duration run of ^{55}Fe exposures was executed. CCD temperatures were controlled by the RTM's internal thermal control loop, whereas the electronics were cooled by conduction to a cold plate stabilized to −60°C. On average, temperatures in the RTM were stable to 0.15 and 0.22°C rms for the CCDs and raft electronics, respectively. Representative time series histories for two RTMs are given in Fig. 9. No secular trends are seen and a significant portion of the variation comes from statistical errors in gain and offset determination. In Fig. 10, we show the gain and offset stability measured for the 144 channels of each of 16 rafts. The gain variations reported in Fig. 10 are well within the requirement of 1% over 12 h, even without correcting for temperature fluctuations. Such corrections can be applied if needed in the final camera

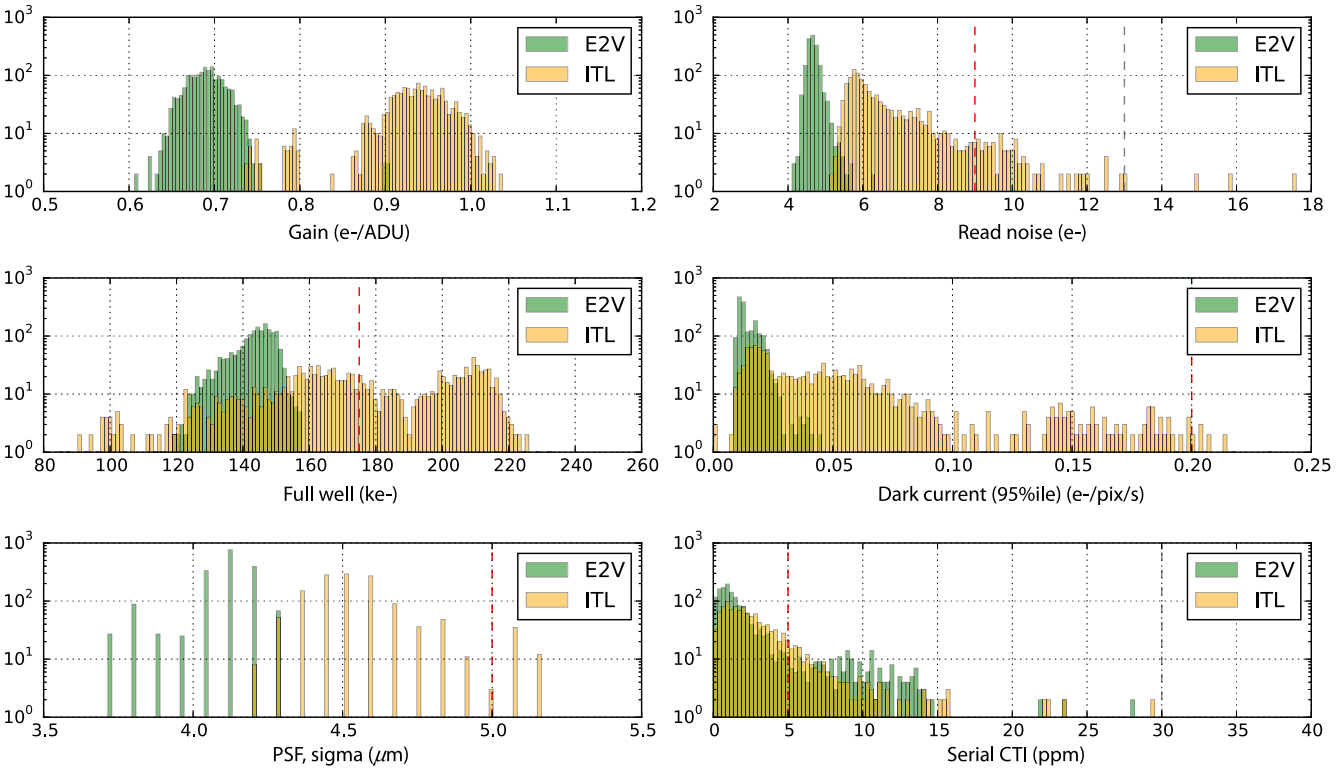

Fig. 3 Histograms of electro-optic parameters: E2V (green) and ITL (orange). Dashed lines indicate hard (red) and soft (gray) specification limits from Table 3. Note: charge diffusion PSF measurement uses coarsely quantized bins.

Table 4 Population statistics and temperature coefficients for all LSST science rafts.

Parameter, P	$\overline{\text{E2V}}$	$\overline{\text{ITL}}$	σ_{E2V}	σ_{ITL}	$\mathrm{d}P/P\mathrm{d}T_{\text{E2V}}$	$\mathrm{d}P/P\mathrm{d}T_{\text{ITL}}$	Unit (tempco)
QE-u	69.8	62.2	6.3	7.8	0.13	0.50	% (%/°C)
QE-g	89.9	88.4	2	3.4	0.027	−0.023	% (%/°C)
QE-r	95.6	94.3	2.4	3.4	−0.017	−0.011	% (%/°C)
QE-i	95.1	99.4	3.6	4.4	−0.016	−0.016	% (%/°C)
QE-z	84.2	92.7	2.4	4.6	0.088	0.063	% (%/°C)
QE-y	25.9	31.5	3.5	4.2	0.51	0.80	% (%/°C)
Read noise	4.7	6.1	0.23	1.8	−0.035	0.09	e^- rms (%/°C)
Gain	0.69	0.94	0.034	0.11	0.023	0.020	e^-/ADU (%/°C)
Full well	144	186	8	40	—	—	ke^- (%/°C)
Dark current 95%	0.013	0.038	0.03	0.048	0.52	−0.20	e^-/pix/s (%/°C)
Diffusion PSF	4.12	4.48	0.14	0.28	—	—	μm rms (%/°C)
CTI-serial	1.52	2.07	6.6	45	—	—	ppm (%/°C)

Note: the gain parameters (row 8) are for the end-to-end signal chain and correspond to about 6.6 and 4.0 μV per electron for E2V and ITL devices, respectively. Temperature coefficients in columns 6 and 7 are estimated from tests performed at focal plane temperatures of −90°C and −100°C. Additional tests, not reported here, confirmed the linear relation between temperature and gain to fractional percent accuracy and measured the variation of selected parameters with respect to the readout electronics temperature.

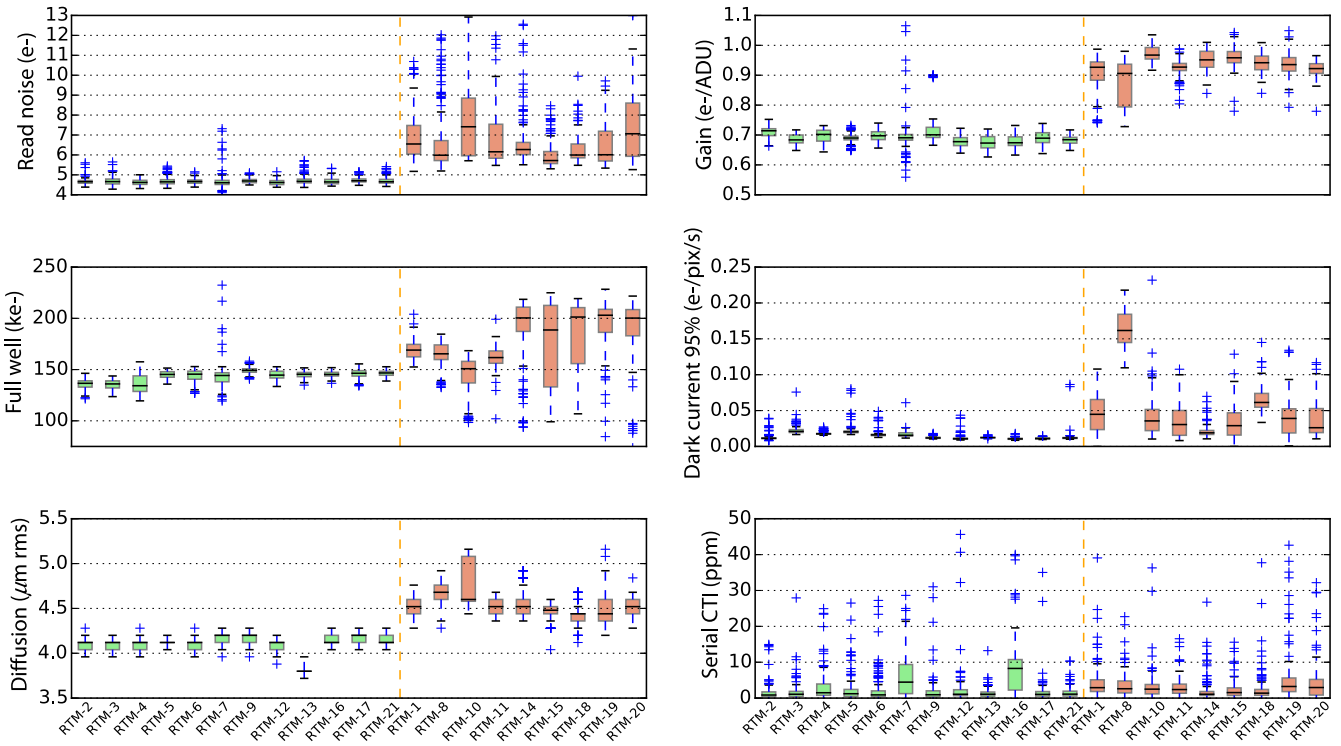

Fig. 4 RTM-by-RTM electro-optic parameters for E2V (green) and ITL (orange) rafts.

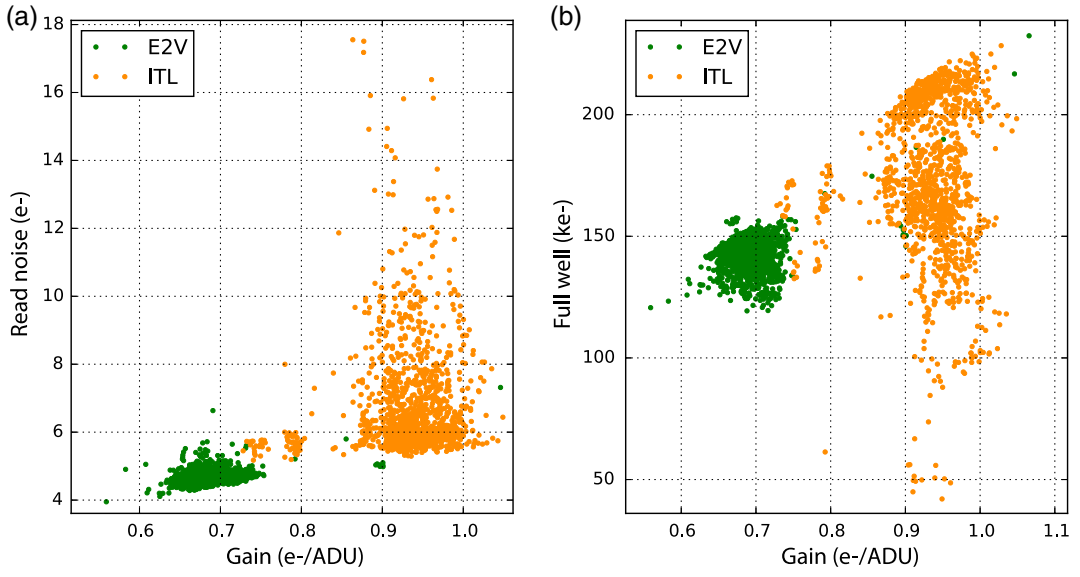

Fig. 5 (a) Correlation between gain and (a) read noise, (b) full-well capacity.

using the temperature coefficients in Table 4. Temperature stability in the final LSST cryostat is expected to be ±0.25°C, corresponding to a gain variation of 0.006%

4 Discussion

The science implications of a mixed-sensor focal plane (e.g., image depth and PSF shape differences, photometric redshift determination, and transient detection) have been discussed in several internal collaboration documents. Although the instrument signature removal pipeline will remove many of the vendor-related performance differences, residuals will remain. In LSST's wide-fast-deep survey, the impact of mixed-FPA non-uniformity is mitigated by the dithering of field centers and sky rotation angles. However, in the deep drilling (DD) fields, repeated exposures will likely be acquired with random sky rotations but only small translational dithering of the field centers. This will result in radial variations in the probability that a DD source will be seen by either sensor type, with the degree of variation depending on the distribution of rafts by supplier type across the focal plane. As an illustration in Fig. 11, we show eight of the many thousand possible arrangements of placing the 8 ITL and 13 E2V rafts in the focal plane. For these

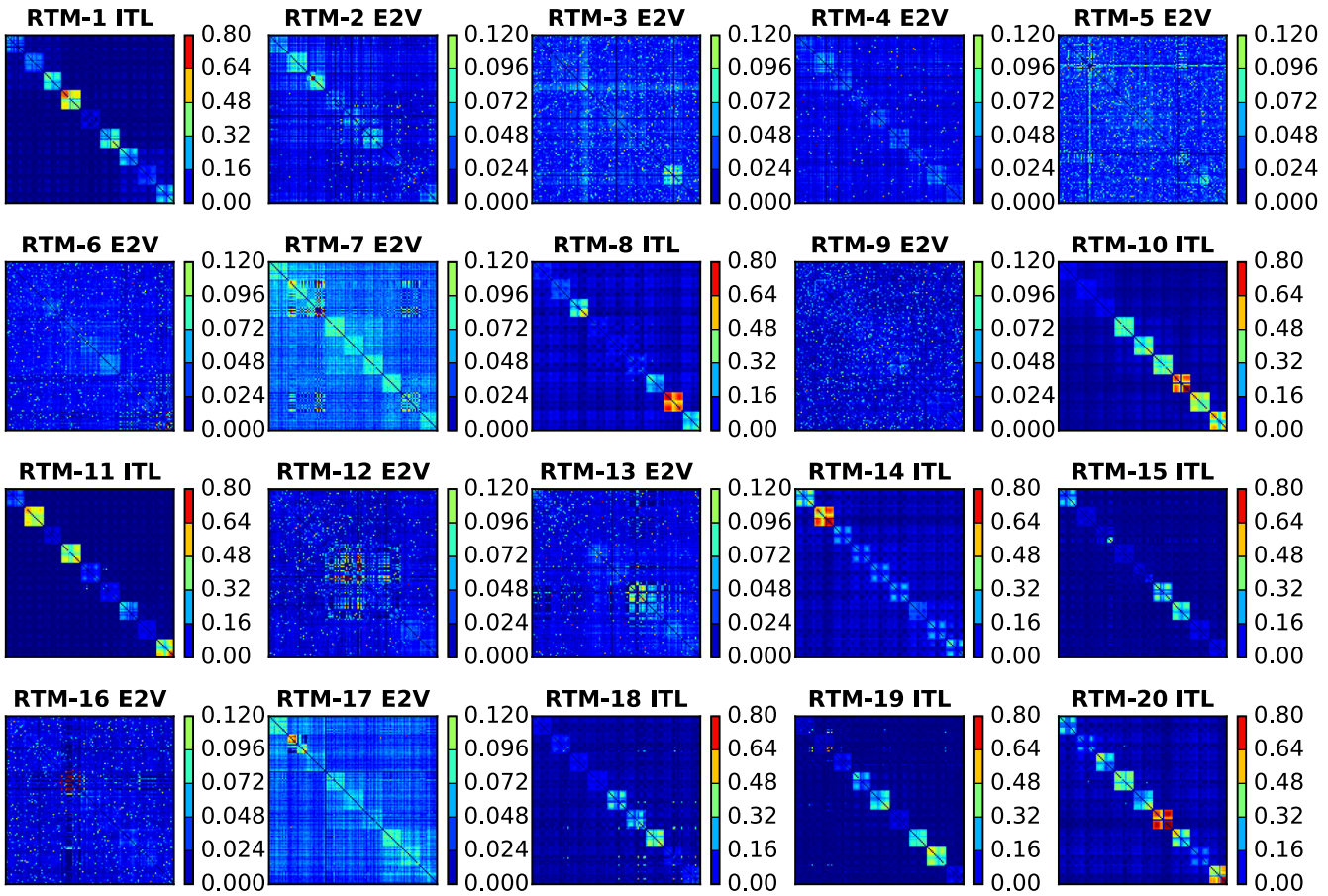

Fig. 6 Noise correlation matrices for 20 RTMs, at 2-s frame readout time. In these plots, the correlation coefficient between all 144×144 channel pairs is shown. The 16×16 block diagonals show the intra-CCD coefficients; the larger 48×48 block diagonals represent the correlations within a single electronics board. Values along the main diagonal = 1 (poorly resolved at this plot scale). Note different scales for E2V and ITL rafts.

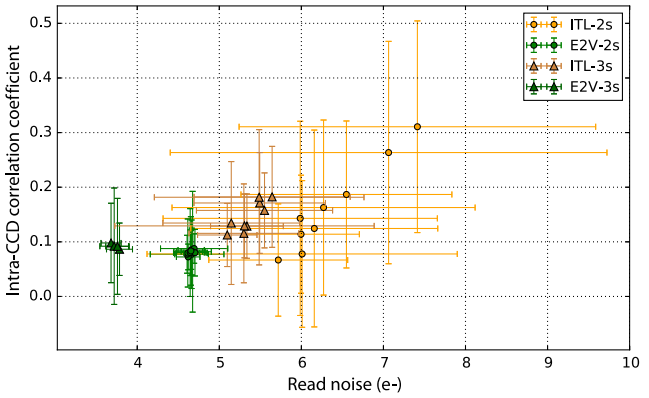

Fig. 7 Read noise (x axis) and intra-CCD correlation for 13 RTMs at 2- and 3-s frame readout times.

configurations, we show in Fig. 12 the azimuthally averaged probability that an object at radius r will be observed by an ITL sensor in the DD fields (blue lines), compared with the FPA-averaged probability of 8/21 (dashed horizontal line).

Figure 11 also shows the number of dissimilar-sensor edges for the eight selected configurations. Analyses that require parameter interpolation across the entire focal plane, if any, may be affected by the number and spatial distribution of such boundaries. From Figs. 11 and 12, it can be seen that configurations E and F minimize both the radial uniformity variation and the number of dissimilar-sensor boundaries compared to the other arrangements.

5 Conclusions

All 21 focal plane modules (rafts) for the 3 Gpixel LSST science focal plane have been constructed and evaluated for electro-optic performance. Population statistics for the main CCD parameters (including temperature coefficients) have been measured. For the ensemble of rafts, median EO performance meets requirements with margin. Dispersion of the EO parameters is strongly tied to the CCD supplier, with the largest differences seen in gain, read noise, dark current, and full well capacity. Increasing the readout time from 2 to 3 s improves the read noise considerably and minimizes the difference between the two sensor types. Gain and offset stability were measured by acquiring x-ray images over 12+ h. Gains remained stable at the 0.1% to 0.2% level while offset variation of only 1 to 2 electrons was observed. The number of dissimilar-CCD boundaries and the azimuthally averaged distribution of the two sensor types about the field center is determined by the placement of the $13 + 8$ rafts in the LSST cryostat.

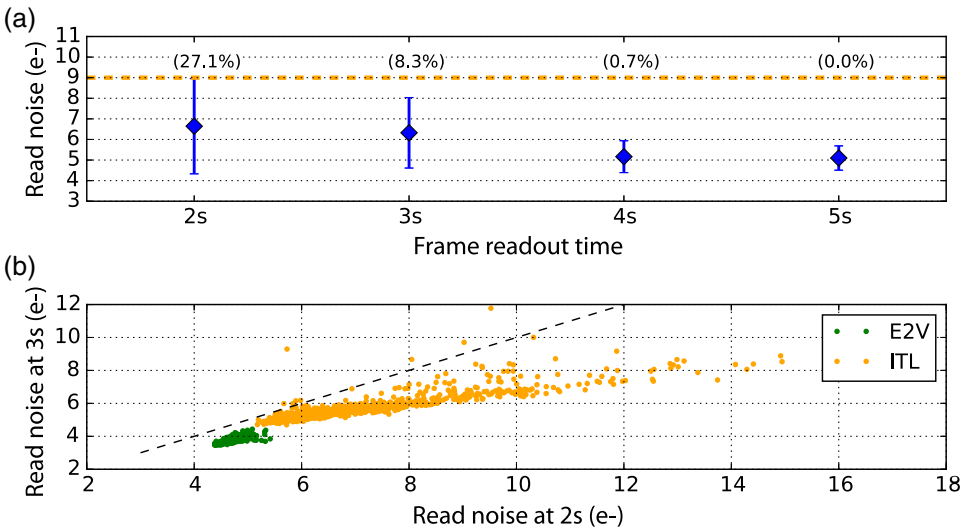

Fig. 8 (a) RTM-10 read noise versus frame readout time. Numbers in parentheses are percent of channels with noise exceeding 9 e^-. Error bars show the channel-to-channel spread in read noise within the raft. (b) Noise results for 13 rafts at 2- and 3-s readout time.

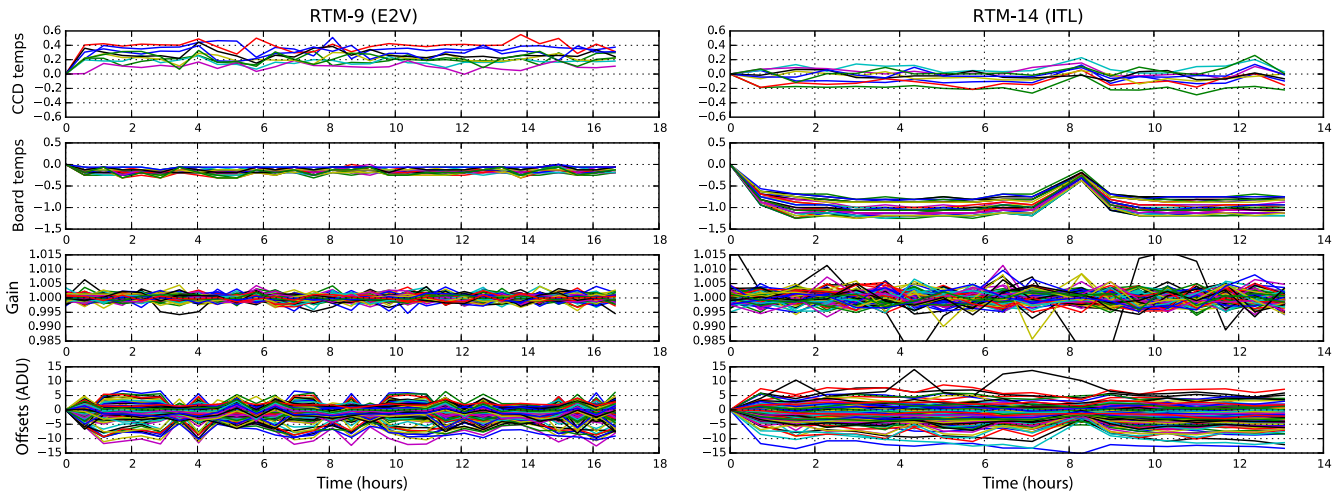

Fig. 9 Time series of CCD temperatures, electronics temperatures, gains, and offsets for RTM-6 (E2V) and RTM-14 (ITL). 144-channel gains are normalized to their mean value throughout the run, temperatures, and offsets are shown as differences from their initial values. Offset refers to the black (zero-signal) level measured at the ADC.

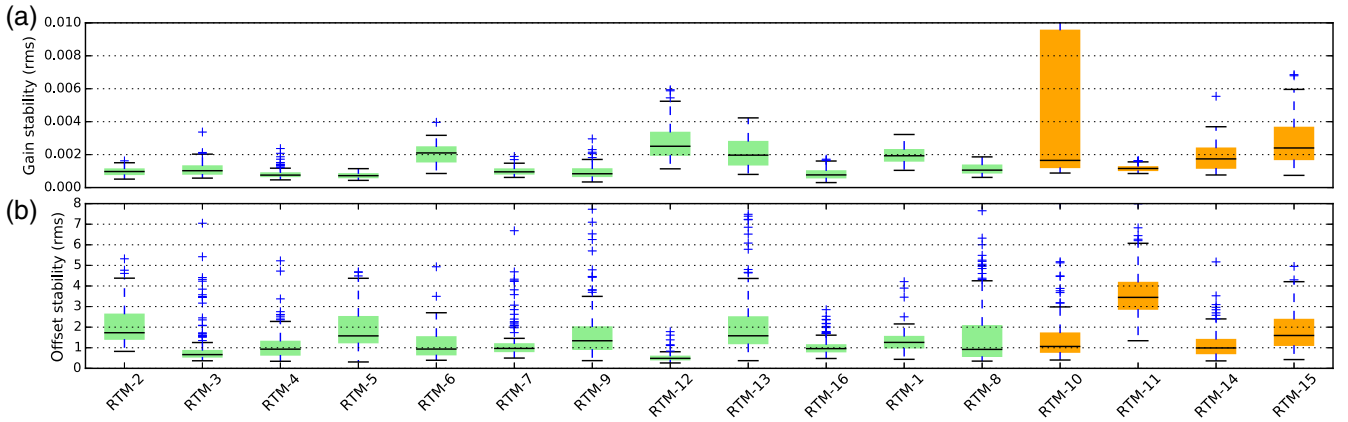

Fig. 10 Long-term stability results for (a) gain and (b) offset of all channels for 12 E2V (green) and 6 ITL (orange) rafts. Error bars represent the spread in stability over the 144 channels of each raft

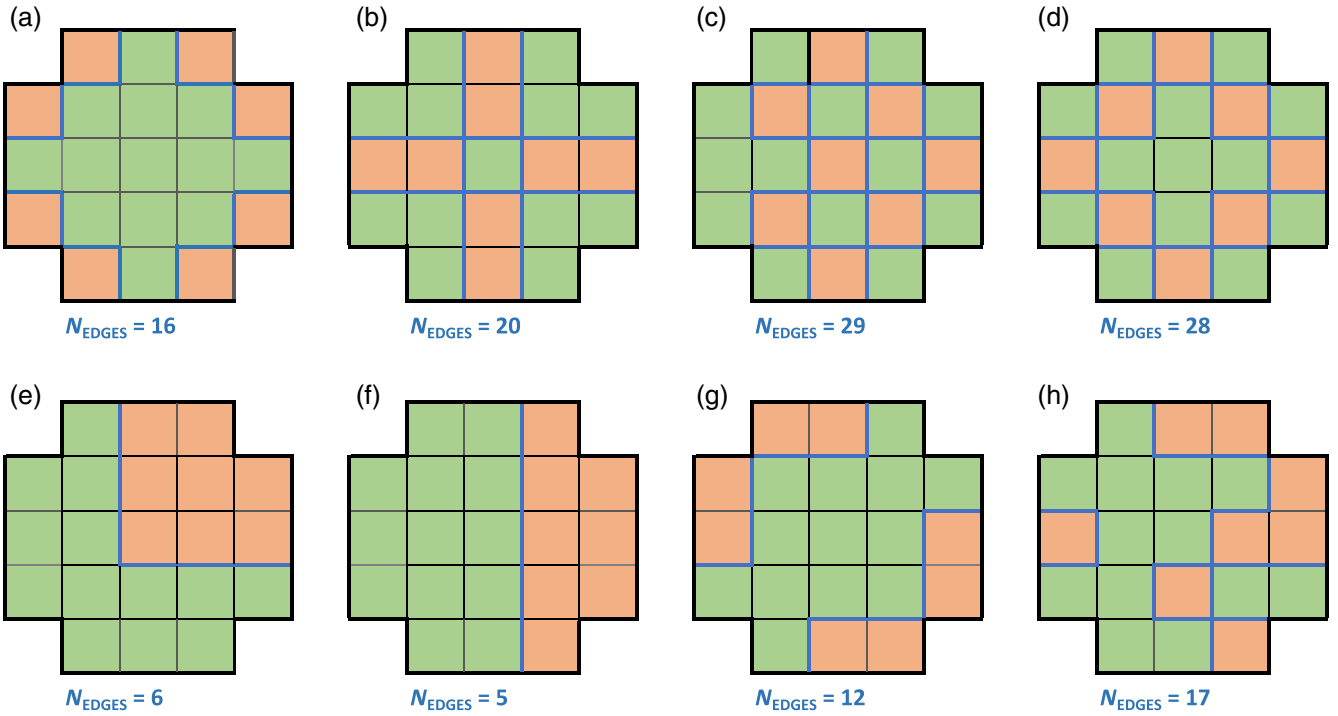

Fig. 11 Panels (a) through (h) illustrate a sample of possible spatial arrangements of 13 E2v (green) and 8 ITL (orange) rafts in the LSST focal plane; number of dissimilar-sensor edges shown in blue.

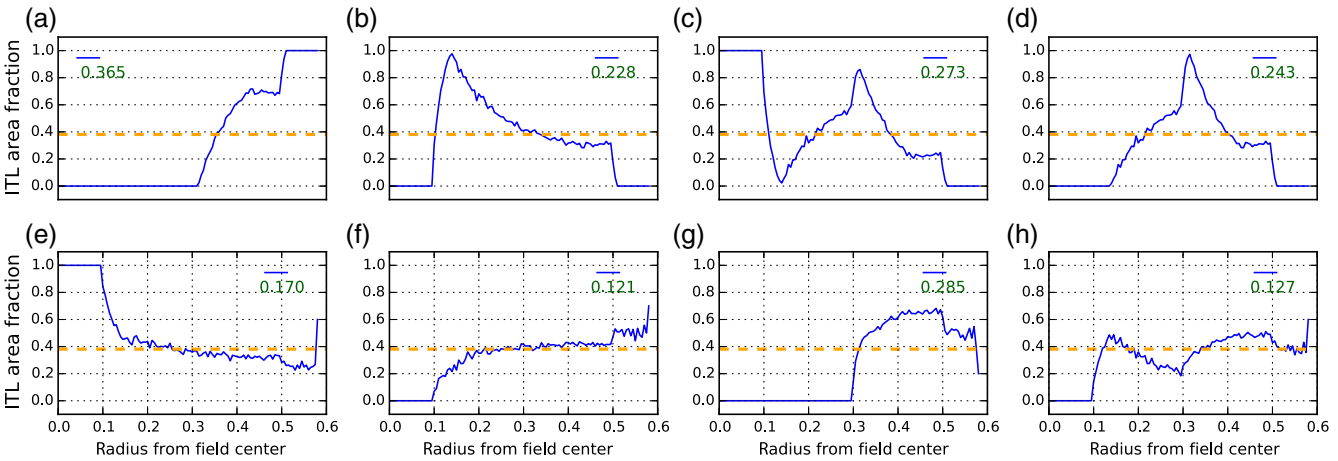

Fig. 12 Azimuthally averaged area fraction occupied by ITL rafts. Panels (a) through (h) correspond to the configurations of Fig. 11. Normalized departure from complete uniformity shown in green for each configuration.

Acknowledgments

Homer Neal, James Chiang, and Claire Juramy-Giles contributed code for EO data acquisition and analysis. The BNL Science Raft Team led by William Wahl maintained and operated the test stand. Their contributions are gratefully acknowledged. This manuscript has been co-authored by employees of Brookhaven Science Associates, LLC, Portions of this work are supported by the Department of Energy under Contract No. DE-SC0012704 with Brookhaven National Laboratory. LSST project activities are supported in part by the National Science Foundation through Governing Cooperative Agreement No. 0809409 managed by the Association of Universities for Research in Astronomy (AURA), and the Department of Energy under Contract No. DE-AC02-76-SFO0515 with the SLAC National Accelerator Laboratory. Additional LSST funding comes from private donations, grants to universities, and in-kind support from LSSTC institutional members.

References

1. Z. Ivezic et al., "LSST: from science drivers to reference design and anticipated data products," *Astrophys. J.* **873**(2), 111 (2009).
2. P. O'Connor et al., "Development of the LSST raft tower modules," *Proc. SPIE* **8453**, 84530L (2012).
3. P. O'Connor et al., "Integrated system tests of the LSST raft tower modules," *Proc. SPIE* **9915**, 99150X (2016).
4. P. Onaka et al., "The Pan-STARRS Gigapixel Camera# 1 and STARGRASP controller results and performance," *Proc. SPIE* **7014**, 70140D (2008).

5. B. Flaugher et al., "The dark energy camera," *Astron. J.* **150**(5), 150 (2015).
6. S. Miyazaki et al., "Hyper Suprime-Cam," *Proc. SPIE* **8446**, 84460Z (2012).
7. S. Kahn et al., "Design and development of the 3.2 gigapixel camera for the large synoptic survey telescope," *Proc. SPIE* **7735**, 77350J (2010).
8. P. O'Connor et al., "Study of silicon thickness optimization for LSST," *Proc. SPIE* **6276**, 62761W (2006).
9. V. Radeka et al., "LSST sensor requirements and characterization of the prototype LSST CCDs," *J. Instrum.* **4**(03), P03002 (2009).
10. S. Russo et al., "The LSST science raft electronics," in *RT2014-19th Real-Time Conf.* (2014).
11. S. Marshall et al., "LSST camera control system," *Proc. SPIE* **6274**, 627422 (2006).
12. A. Perazzo et al., "Camera data acquisition for the large synoptic survey telescope," in *2007 15th IEEE-NPSS Real-Time Conf.*, IEEE, pp. 1–2 (2007).
13. M. Jurić et al., "The LSST data management system," arXiv:1512 .07914.
14. J. R. Janesick et al., *Scientific Charge-Coupled Devices*, vol. **117**, SPIE Press, Bellingham, Washington, DC (2001).
15. A. Snyder, K. Gilmore, and A. Roodman, "Optimization of CCD operating voltages for the LSST camera," *Proc. SPIE* **10709**, 107092B (2018).
16. P. Astier, "An introduction to some imperfections of CCD sensors," *J. Instrum.* **10**(05), C05013 (2015).
17. P. O'Connor, "Crosstalk in multi-output CCDs for LSST," *J. Instrum.* **10**(05), C05010 (2015).
18. P. Antilogus et al., "The brighter-fatter effect and pixel correlations in CCD sensors," *J. Instrum.* **9**(03), C03048 (2014).
19. A. Guyonnet et al., "Evidence for self-interaction of charge distribution in charge-coupled devices," *Astron. Astrophys.* **575**, A41 (2015).
20. R. Coles et al., "An automated system to measure the quantum efficiency of CCDs for astronomy," *J. Instrum.* **12**(04), C04014 (2017).

Paul O'Connor is a senior scientist at Brookhaven National Laboratory. He obtained his PhD in physics from Brown University, in 1980 and worked as a member of technical staff at AT&T Bell Laboratories for 10 years before moving to Brookhaven. His research interests include radiation detectors, low-noise signal processing, and developing instrumentation systems for particle and astroparticle physics.